



Uniform porous spinel NiCo_2O_4 with enhanced electrochemical performances



Zhibin Wu^a, Xuli Pu^b, Yirong Zhu^a, Mingjun Jing^a, Qiyuan Chen^a, Xinnan Jia^a, Xiaobo Ji^{a,*}

^aDepartment of Chemistry and Chemical Engineering, Central South University, Changsha 410083, China

^bXiamen Entry-Exit Inspection and Quarantine Bureau of People's Republic of China, Xiamen 361000, China

ARTICLE INFO

Article history:

Received 22 October 2014

Received in revised form 14 January 2015

Accepted 21 January 2015

Available online 29 January 2015

Keywords:

Nickel cobaltite

Co-precipitation

Porous

Electrochemistry

Supercapacitor

ABSTRACT

The electrochemical performances of uniform porous NiCo_2O_4 nanoparticles obtained through a template-free co-precipitation way were explored in details, revealing that NiCo_2O_4 electrode prepared by NaHCO_3 has a great advantage over that fabricated by NaOH , resulting in more uniform and higher porous nanostructures, which manifests a superior specific capacitance of 726.8 F g^{-1} at 1 A g^{-1} and a better cycle stability of 72.7% retention at 5 A g^{-1} after 2000 cycles. The enhanced pseudocapacitive performances can mainly be ascribed to well-distributed mesoporous structure coming from the releasing of CO_2 that primarily prevents the agglomeration of the nanocrystals. Therefore, it can be a promising candidate to substitute the routine precipitant of NaOH for the preparation of some other binary or even ternary metal oxides for supercapacitors.

© 2015 Elsevier B.V. All rights reserved.

1. Introduction

Electrochemical capacitors known as supercapacitors are advantageous to rapid power delivery and recharging, which are widely applied in hybrid electric vehicles, memory back-up devices, industrial power system and electronic products [1]. Transition metal oxides with mesoporous structures are very attractive materials for supercapacitors because of their high specific surface areas and fast redox reactions. Note that multiple oxidation states and high surface areas are in favor of achieving much higher energy density and better power density [2,3].

Spinel nickel cobaltites (NiCo_2O_4), which are a kind of novel pseudocapacitive material with outstanding electrochemical capacitive performances, have attracted great attention due to its tremendous advantages including high specific capacity, good rate capacity and excellent cycling performance [4,5]. As a powerful candidate material for supercapacitor, nickel cobaltite possesses richer electroactive sites and at least two magnitudes higher electrical conductivity than that of NiO and Co_3O_4 , and shows comparable capacitive performances with noble metal oxides of RuO_2 . In addition, it has some other advantages such as more abundant resources and much lower costs than RuO_2 [3]. As firstly reported by Hu et al. [4,6], spinel NiCo_2O_4 aerogels fabricated by a sol-gel

method demonstrated an ultrahigh specific capacitance of 1400 F g^{-1} , while $\text{RuO}_2 \cdot n\text{H}_2\text{O}$ nanoparticles prepared by a sol-gel method exhibited a similar specific capacitance of 1580 F g^{-1} . Thus, NiCo_2O_4 is playing an important role in complementing or replacing electrode materials such as NiO , Co_3O_4 and RuO_2 in energy storage field. Recently, great progress has been made in the enhancement of its electrochemical performances and many researchers are dedicating to preparing various unique morphologies such as hollow spheres [7], hollow rods [8] and core/shell structures [9]. Even so, structural tailoring is still beneficial since tuned structure, the as-resulting surface chemistry and porosity could further optimize the electrochemical performances of the electrodes [10,11]. Large specific surface areas could provide more electrolyte ion accumulation, while highly ordered and suitable pore sizes facilitate to acquire better mechanical stability and higher surface utilization ratio, resulting in a large improvement of specific capacity and rate capacity. In addition, mesoporous nanostructures with controlled porosity benefit from the dispersion of the active phase and the accessibility of the electrolyte [10]. Therefore, unique structures consisting of uniform mesoporous nanoparticles will obtain more remarkable electrochemical performances.

As far as we know, mesoporous nanostructures with uniform pore size are usually prepared with template-directed methods such as mesoporous silica or carbon [7], surfactants [12,13] and long-chain polymers [14]. However, some uncertainty obstacles,

* Corresponding author. Tel./fax: +86 731 88879616.

E-mail address: xji@csu.edu.cn (X. Ji).

such as the residual templates in the resultant samples and the fussy multistep procedures, always harass these methods [15]. Moreover, spinel nickel cobaltite, in general, is mostly prepared by using sodium hydroxide as precipitant and other surfactants as auxiliaries, which is complex to control and difficult to effectively disperse those nanoparticles [12,16,17].

In this present work, spinel NiCo_2O_4 samples were obtained via a template-free co-precipitation method by utilizing different precipitants of NaHCO_3 (SBC) and NaOH (SHO). The distinctive effect of NaHCO_3 on the electrochemical performances of NiCo_2O_4 was, for the first time, elaborated in details. In addition, it is worth noting that the uniform porous NiCo_2O_4 prepared by NaHCO_3 (NiCo_2O_4 (SBC)) has exhibited a better pseudocapacitive performances than that of the NiCo_2O_4 prepared by NaOH (NiCo_2O_4 (SHO)).

2. Experimental

2.1. Materials and chemicals

All the chemicals used in the experiments were of analytical grade and were used without further purification. $\text{Ni}(\text{Ac})_2 \cdot 4\text{H}_2\text{O}$ (analytical grade) was purchased from Fengchuan Chemical Reagent Co., Ltd, Tianjin. $\text{Co}(\text{Ac})_2 \cdot 4\text{H}_2\text{O}$ (analytical grade) was purchased from Xilong chemical Co., Ltd. Sodium bicarbonate (analytical grade) and sodium hydroxide (analytical grade) were bought from Hengxing Co., Ltd, Tianjin. All solutions were prepared with distilled water of resistivity not less than $18.2 \text{ M}\Omega \text{ cm}$ (Synergy UV, Millipore).

2.2. Preparation of NiCo_2O_4

$\text{Ni}(\text{Ac})_2 \cdot 4\text{H}_2\text{O}$ (5 mmol) and $\text{Co}(\text{Ac})_2 \cdot 4\text{H}_2\text{O}$ (10 mmol) were first dissolved in distilled water (100 mL) to form a solution. After being magnetically stirred for 15 min, NaHCO_3 (30 mmol, 100 mL) was added dropwise as precipitant at room temperature under constant magnetic stirring. The resulting suspension was kept stirring for another 3 h. Then, the precipitates were collected by filtration, washed several times with deionized water and absolute ethanol, and finally dried on a watch glass at 50°C overnight. At last, the dried precursor was further annealed at 300°C under air atmosphere for 2 h with a heating rate of 2°C min^{-1} to obtain NiCo_2O_4 (SBC).

By contrast, NaOH was also used as precipitant to prepare NiCo_2O_4 (SHO) following the same route.

2.3. Materials characterization

X-ray diffraction (XRD) patterns were collected on a Rigaku D/max 2550 VB* 18 kW X-ray diffractometer with Cu K α radiation (0.1542 nm) at a scanning rate of $0.1^\circ 2\theta \text{ s}^{-1}$. The Fourier transform infrared spectrophotometer (FT-IR, AVTATAR, 370) was measured in the frequency range from 400 cm^{-1} to 4000 cm^{-1} with KBr as a reference to analyze the chemical structure. Field-emission scanning electronic microscopy (FESEM, JSM-6700F), transmission electron microscopy (TEM, JEM-2100F), high resolution transmission electron microscopy (HRTEM, JEM-2100F) and the corresponding selected area electron diffraction (SAED) were performed to characterize the morphologies and structures. Thermogravimetric analysis (TGA) and differential scanning calorimetry (DSC) were carried out on a thermal analysis instrument (NETZSCH STA449F3) at a heating rate of $10^\circ\text{C min}^{-1}$ from 40°C to 800°C in air. The Brunauer–Emmett–Teller (BET, BELSORP-MINIII) specific surface area was obtained from the N_2 adsorption/desorption isotherm recorded at 77 K and the pore size distribution was evaluated by using the Barrett–Joyner–Halenda (BJH) model.

2.4. Electrochemical characterization

For electrochemical measurements, the working electrode consisted of NiCo_2O_4 , acetylene black, and polyvinylidene difluoride (PVDF) in a weight ratio of 70:20:10 and the prepared mixture were then pressed onto a foam nickel under a pressure of 10 MPa for 30 s. The loading mass of the electroactive materials was about 1 mg cm^{-2} . When used as a current collector, nickel foam was rinsed with deionized water, acetone and ethanol twice in an ultrasonic bath, respectively. Finally, it was dried in a vacuum oven at 80°C for 8 h. A three electrode system consisted of the fabricated working electrode, platinum counter electrode and Hg/HgO reference electrode was employed in 2 M KOH aqueous solution. All measurements including cyclic voltammetry (CV), galvanostatic current charge–discharge, cycle life test and electrochemical impedance spectroscopy (EIS) were conducted with a Modulab (Solartron Analytical) electrochemical workstation in the three electrode system.

3. Results and discussion

3.1. Structural characterization

Crystalline structures of those two as-obtained NiCo_2O_4 prepared by different precipitants were studied by X-ray diffraction and the corresponding XRD patterns are shown in Fig. 1. The diffraction peaks of 18.91° , 31.15° , 36.70° , 38.40° , 44.62° , 55.44° , 59.09° , 64.98° and 68.31° can be indexed as the (111), (220), (311), (222), (400), (422), (511), (440) and (531) crystal planes of NiCo_2O_4 (JCPDS Card No. 20-0781). It can be observed that all peaks in the two patterns can match perfectly for the face-centered cubic structured NiCo_2O_4 with a space group of Fd3m (JCPDS Card No. 20-0781). No peak from other crystallized phases can be detected, indicating the high purity of NiCo_2O_4 products after calcination. The average crystal sizes of NiCo_2O_4 prepared by NaOH and NaHCO_3 are respectively calculated to be 15.1 and 10.0 nm according to the following Scherer's formula:

$$D = (0.89 \times \lambda) / (\beta \times \cos \theta) \quad (1)$$

where D is the crystallite size, 0.89 is the Debye–Scherrer constant, λ represents the X-ray wavelength, β is the full width at half maximum, and θ is the Bragg diffraction angle. The smaller average crystal size of NiCo_2O_4 (SBC) can be interpreted from the XRD patterns in which the width of the diffraction peak is broader. The crystal sizes are further confirmed by TEM and HRTEM, suggesting that NaHCO_3 may contribute to the production of nanoparticles with smaller crystal size, resulting in better electrochemical performance.

DSC and TGA curves of the NiCo_2O_4 precursor prepared by NaOH are shown in Fig. 2a, while the curves of the NiCo_2O_4 precursor obtained by NaHCO_3 are displayed in Fig. 2b. Fig. 2a demonstrates three significant weight loss steps in thermogravimetric plots. The first weight loss step occurring between 40 and 185°C with two endothermic peaks at 64.7 and 162.4°C in the DSC curves is attributed to the loss of surface adsorbed water and crystalline water molecules. The second weight loss step occurring between 185 and 246°C and the third weight loss step occurring between 246 and 362°C in the DSC curves (14.53% in total) are probably attributed to two different reaction rates of the conversion process from Ni–Co hydroxides precursor to spinel NiCo_2O_4 , which could correspond to two continuous but difform exothermic peaks at 211.5 and 353.1°C , respectively [18]. Note that the calculated weight loss of 14.53% is close to the theoretical weight loss of 13.67%. As the temperature increases (above 362°C), it is possible

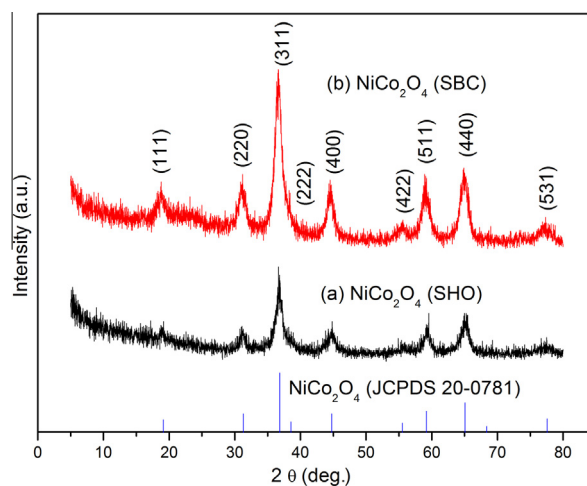


Fig. 1. XRD patterns of the two NiCo_2O_4 samples prepared by different precipitants.

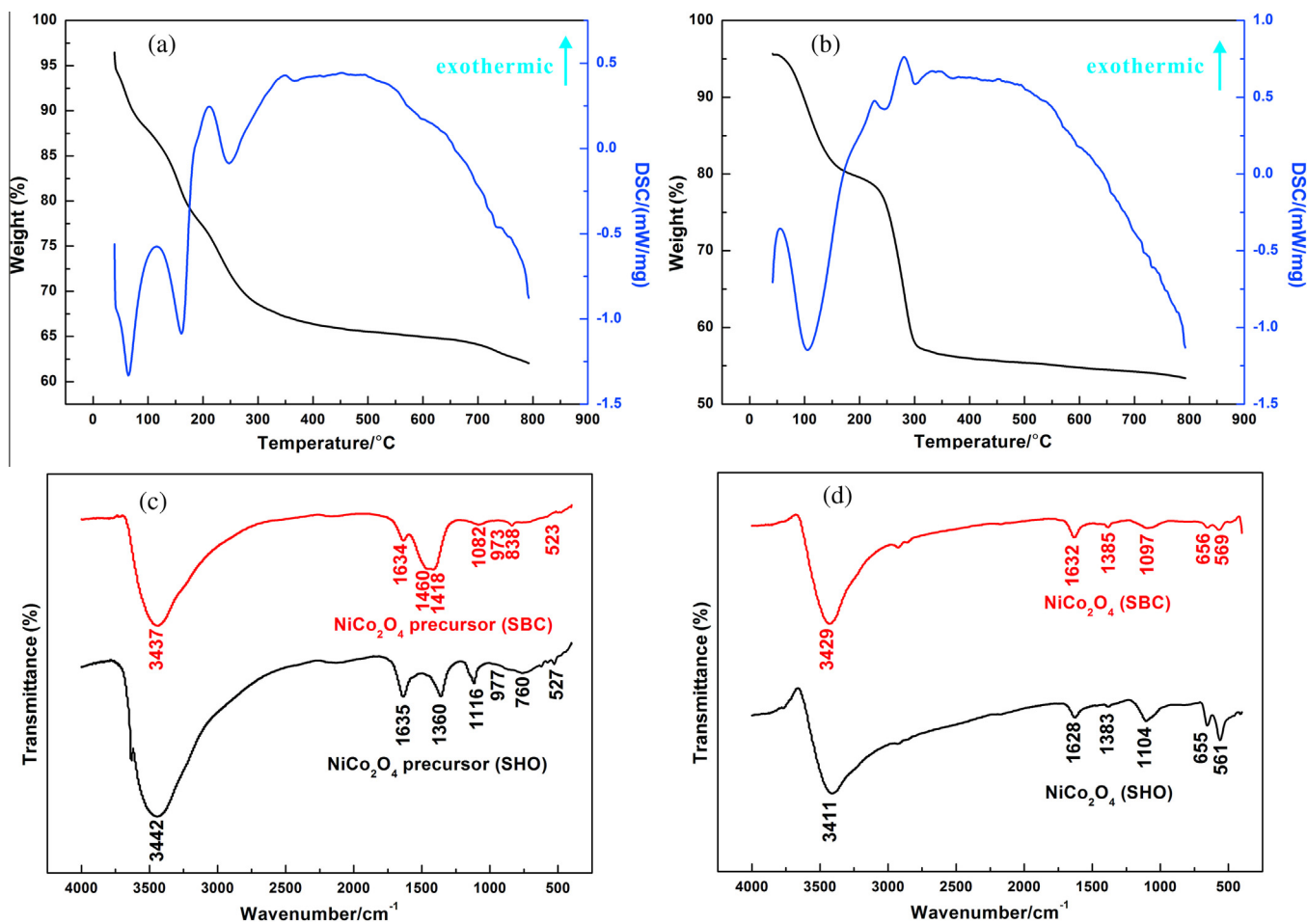


Fig. 2. DSC-TGA curves of the NiCo₂O₄ precursors prepared by different precipitants: (a) NiCo₂O₄ (SHO) and (b) NiCo₂O₄ (SBC). FT-IR spectra: (c) NiCo₂O₄ precursor prepared by SHO and SBC. (d) NiCo₂O₄ prepared by SHO and SBC.

that the amorphous sample may transform from amorphous solid to better crystalline solid with a broad exothermic peak in the DSC signal. Then, it starts to decompose into NiO and Co₃O₄ obviously at 727.2 °C with an endothermic peak at 731.9 °C and certain weight loss is also reflected in the TGA curve [21]. Fig. 2b shows three significant weight loss steps in thermogravimetric plots. The first significant weight loss step occurs between 40 and 191 °C with an endothermic peak at 104.5 °C in the DSC curves, which is due to the evaporation of crystal water. The second and third weight loss step (27.45% in total) occurred between 191 and 300 °C with two endothermic peaks respectively at 226 and 280.8 °C in the DSC curves may be one of the decomposition process transforming Ni-Co hydroxide carbonates precursor to spinel NiCo₂O₄. While the fourth and fifth slight weight loss (2.03% in total) occurring between 300 and 370.5 °C with two exothermal peak at 332 and 344 °C may be the other decomposition process changing Ni-Co hydroxide carbonates to spinel NiCo₂O₄. The whole weight loss of 29.48% is smaller than the theoretical weight loss of 32.54% calculated by NiCo₂(CO₃)₃ precursor, while it is larger than the theoretical weight loss of 13.64% calculated by NiCo₂(OH)₆ precursor. Thus, the precursor could be speculated to be NiCo₂(OH)_{3x}(CO₃)_(3-1.5x). It seems that the conversion process of two different reaction rates also happened in this precursor. As the temperature increases (above 370.5 °C), it is possible that the amorphous sample may transform from amorphous solid to better crystalline solid with a broad exothermic peak in the DSC

signal and the possibility of some peaks caused by the slight decomposition of NiCo₂O₄ above 400 °C could not be ruled out [4,19,20]. After that, as the temperature increase, it also starts to decompose into NiO and Co₃O₄ with some minor peaks [21]. It is reported that when calcination temperature of Ni-Co precursor increases from 250 °C to 400 °C, the corresponding specific surface area and specific capacitance of NiCo₂O₄ decrease in the similar trend [22]. Meanwhile, spinel NiCo₂O₄ may not be stable when temperature is higher than 400 °C [4,19,20]. Those two samples exhibit significant weight loss below 300 °C in the TGA curves, and then the calcination temperature for those two samples is selected as 300 °C in order to obtain pure spinel NiCo₂O₄ with relatively large specific surface areas and high specific capacitance.

FT-IR spectra were utilized to study the structural molecular changes of the NiCo₂O₄ samples before and after calcination. The FT-IR spectra of the NiCo₂O₄ precursor prepared by NaOH and NaHCO₃ are shown in Fig. 2c and corresponding enlarged drawing are provided in Fig. S1, while the FT-IR spectra of spinel NiCo₂O₄ prepared by NaOH and NaHCO₃ are shown in Fig. 2d. As shown in Fig. 2c, the NiCo₂O₄ precursor prepared by NaOH shows the peaks at around 3442 (strong) and 1635 cm⁻¹ (shoulder), respectively, corresponding to the stretching vibration of hydrogen-bonded hydroxyl groups and the bending mode of absorbed water molecules [23], while the weak peaks at 527 and 977 cm⁻¹ exhibit the characteristic absorption peaks of metal-OH vibrations [24,25]. Based on the analysis above, the precursor prepared by NaOH can

be identified as a typical Ni–Co hydroxide. For the NiCo_2O_4 precursor prepared by NaHCO_3 , the infrared absorption spectra of inorganic carbonate adsorption bands are distinctive as the strong, characteristic absorptions can be found at around 838 (ν_2 mode), 1082 (ν_1 mode), 1418 and 1460 cm^{-1} (ν_3 mode) [20,26]. Besides, it also shows weak absorption peaks of metal–OH vibrations at the peaks 523 and 973 cm^{-1} . Therefore, these results indicate that the precursor of $\text{NiCo}_2(\text{OH})_{3x}(\text{CO}_3)_{3-1.5x}$ is formed under the hydrolysis of NaHCO_3 , which is in good agreement with the work reported by the groups of Tseng [27] and Wang [28]. In Fig. 2d, similar behaviors are observed in those two as-obtained NiCo_2O_4 and the characteristic absorption peaks of metal–oxygen vibrations are at 655 (656) and 561 (569) cm^{-1} [24,29], which further demonstrate the formation of pure NiCo_2O_4 by annealing at 300 °C.

The morphologies of the as-obtained samples were investigated by SEM and TEM with different magnifications. Fig. 3a–c displays SEM images of NiCo_2O_4 prepared by NaOH and its corresponding TEM images were shown in Fig. 4a and b. Clearly, the observed NiCo_2O_4 sample is composed of disordered nanoparticles with large agglomerates and rough surfaces. Moreover, its interplanar spacing in Fig. 4c is 0.47 and 0.25 nm, matching well with the (111) and (311) lattice planes of NiCo_2O_4 , respectively. However, SEM images of NiCo_2O_4 prepared by NaHCO_3 exhibit fluffy mesoporous

structures in Fig. 3d–f, and TEM images in Fig. 4d–f further display its uniform sizes and good dispersion, which is consistent with the results obtained from pore size distribution in the following BET analysis. Furthermore, HRTEM image (Fig. 4g) reveals that spacing between adjacent fringes is 0.29 and 0.25 nm, which can respectively be assigned to theoretical interplanar spacing of spinel NiCo_2O_4 (220) and (311) planes. The SAED pattern (Fig. 4h) of NiCo_2O_4 prepared by NaHCO_3 suggests the polycrystalline nature of the NiCo_2O_4 nanoparticles. By comparing those two samples, we conclude that the different morphologies can be attributed to the effect of different precipitants.

Our approach for uniform porous NiCo_2O_4 utilizing as pseudocapacitive electrode mainly involves two steps, namely formation of Ni–Co hydroxide carbonates precursor and thermal decomposition of the precursor into spinel oxides. It is well known that sodium bicarbonate aqueous solutions are mildly alkaline due to the formation of carbonic acid and hydroxide ion and it tends to slowly generate carbon dioxide even under room temperature with continuous stirring [30]. In presence of Co^{2+} and Ni^{2+} , the speed of the hydrolyzation becomes much faster so that more carbon dioxide is released. As a result, dissolved carbon dioxide generates much carbonate ions and hydroxide ion, causing the formation of Ni–Co hydroxide carbonates precursor. In addition, carbon dioxide

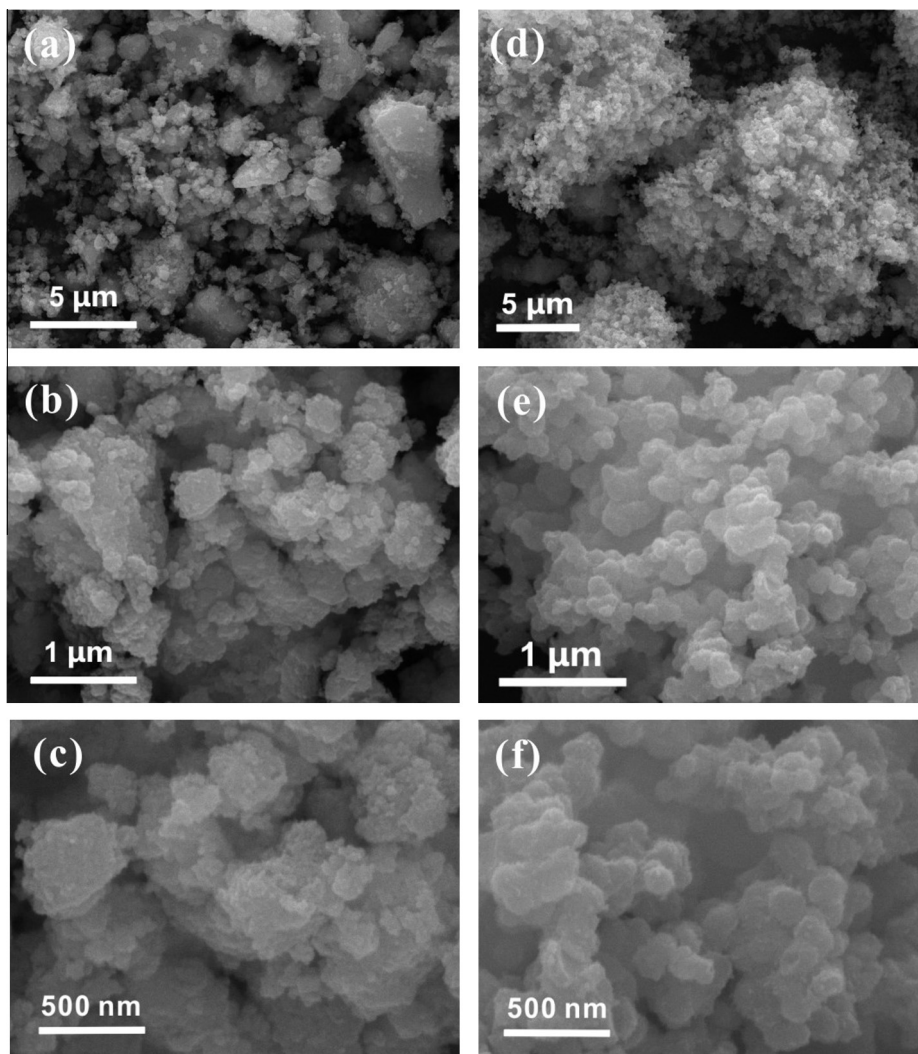


Fig. 3. SEM images of NiCo_2O_4 prepared by different precipitants: (a)–(c) NiCo_2O_4 (SHO); (d)–(f) NiCo_2O_4 (SBC).

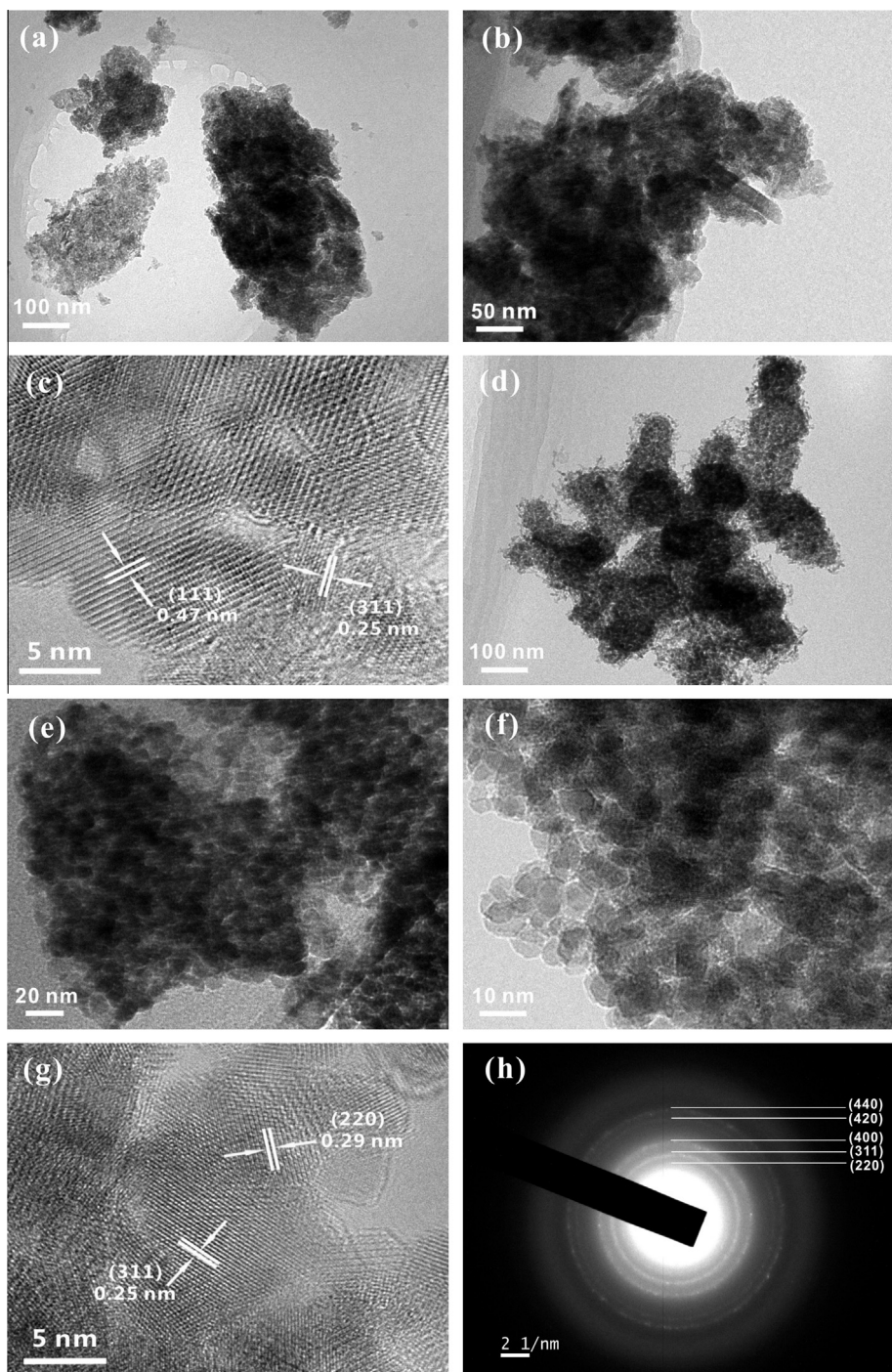
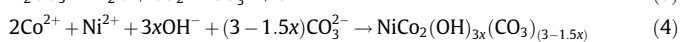


Fig. 4. TEM images of NiCo_2O_4 prepared by different precipitants: (a) and (b) NiCo_2O_4 (SHO); (d)–(f) NiCo_2O_4 (SBC). HRTEM images of NiCo_2O_4 prepared by different precipitants: (c) NiCo_2O_4 (SHO) and (g) NiCo_2O_4 (SBC). (h) SAED pattern of NiCo_2O_4 (SBC).

gas bubbles could provide aggregation centers for the reaction, creating loose hydroxide carbonates precursor through slowly dropping process [31,32]. Once calcinated, the hydroxide carbonates precursor decompose into CO_2 and H_2O , refining the particle size and increasing the porosity of the powder [33]. The reaction process [34,35] could be expressed as:



As shown in Fig. 5, BET specific surface areas of NiCo_2O_4 were performed by N_2 adsorption–desorption isotherms at 77 K, and the corresponding pore size distributions were calculated by Barrett–Joyner–Halenda (BJH) method from the desorption branch. Primary structural parameters are derived from the isotherms and tabulated in Table 1. Those two samples exhibit a hysteresis loop and BET specific surface areas of the NiCo_2O_4 prepared by NaOH and NaHCO_3 are calculated to be 132.6 and 141.7 $\text{m}^2 \text{g}^{-1}$ according to the multi-point BET equation, respectively. The pore size distributions are displayed in the insets of Fig. 5. Fig. 5a manifests the disordered mesoporous structure of the NiCo_2O_4 (SHO)

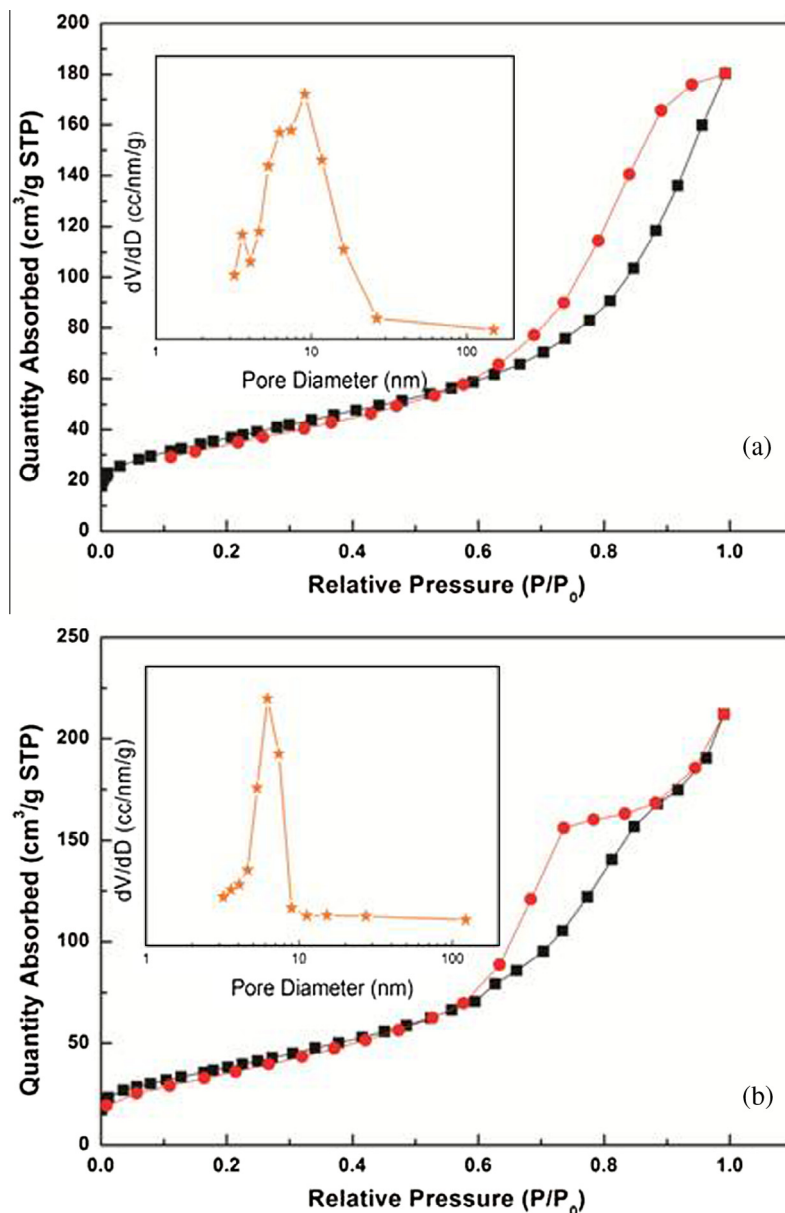


Fig. 5. Nitrogen adsorption and desorption isotherms of NiCo_2O_4 prepared by different precipitants: (a) NiCo_2O_4 (SHO); (b) NiCo_2O_4 (SBC). The insets show the corresponding BJH pore size distributions.

Table 1
Structural parameters of NiCo_2O_4 prepared by NaOH and NaHCO_3 , respectively.

Samples	BET specific surface area ($\text{m}^2 \text{g}^{-1}$)	BJH pore volume ($\text{cm}^3 \text{g}^{-1}$)	BJH pore size (nm)
NiCo_2O_4 (SHO)	132.6	0.28	9.1
NiCo_2O_4 (SBC)	141.7	0.33	6.2

with a broad pore-size distribution (4–26 nm) centered at around 9.1 nm, while the total pore volume is calculated as $0.28 \text{ cm}^3 \text{ g}^{-1}$. Moreover, it is worth noting that a small part of macroporous structures are also observed in the inset, which results from the aggregation of the nanoparticles. Compared with the inset of Fig. 5a, the inset of Fig. 5b indicates that the uniform mesoporous

structure of the NiCo_2O_4 (SBC) with a narrow pore-size distribution (5–9 nm) is centered at around 6.2 nm, and the total pore volume is calculated as high as $0.33 \text{ cm}^3 \text{ g}^{-1}$. Such a uniform pore structure is particularly in favor of fast charging–discharging process for supercapacitors because uniform mesoporous structure with a high surface area and a large pore volume could facilitate the diffusion of electrolyte ion and charge transfer, and thus providing more electroactive sites for energy storage. This type of structure is closely linked with the introduction of foaming agent of NaHCO_3 which could keep a mild reaction environment and generate abundant carbon dioxides. In conclusion, we can see that the characters of pore structure of NiCo_2O_4 (SBC) is better than NiCo_2O_4 (SHO) in providing higher specific surface area, better pore volume and pore size distribution and it is reasonable to expect the differences of the two samples in electrochemical performances.

3.2. Electrochemical characteristics

Fig. 6a and b shows CV measurements for NiCo₂O₄ (SHO) and NiCo₂O₄ (SBC) from 0 to 0.55 V at scanning rates of 2–20 mV s⁻¹, respectively. Two well-defined pairs of redox current peaks can be found in each voltammogram, which clearly reveal that the capacitive characteristics of the NiCo₂O₄ electrodes are mainly governed by Faradaic redox reactions. As reported in some literatures [36,37], there exist valence state changes of Co³⁺/Co⁴⁺ and M²⁺/M³⁺

(M = Co or Ni) on the surface of the electrode materials and the electrochemical redox potentials of the M²⁺/M³⁺ and Co³⁺/Co⁴⁺ transitions are so close that the redox peaks observed is becoming an overlapping one, which is consistent with our work. Its pseudocapacitive behavior [4,38] in the KOH solution can be described as the following equations:

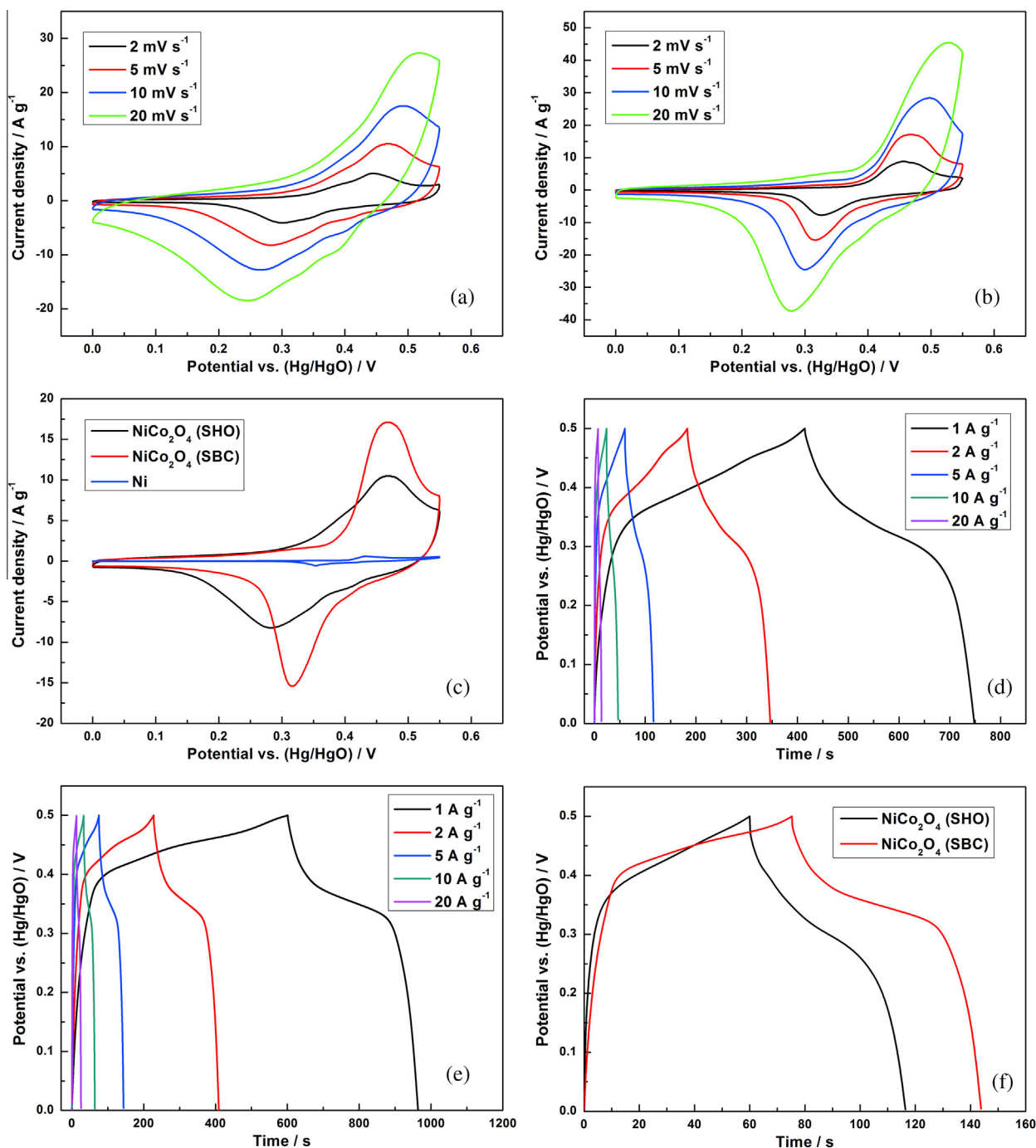
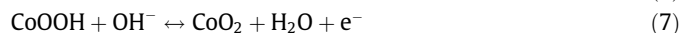
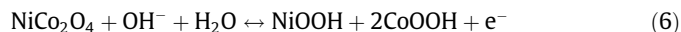


Fig. 6. CV curves of the NiCo₂O₄ electrodes prepared by different precipitants at various scan rates: (a) NiCo₂O₄ (SHO); (b) NiCo₂O₄ (SBC); (c) comparison of CV curves of the NiCo₂O₄ (SHO) electrode, NiCo₂O₄ (SBC) electrode and Ni electrode at a scan rate of 5 mV s⁻¹. Galvanostatic charge–discharge curves of the NiCo₂O₄ electrodes prepared by different precipitants at various current densities: (d) NiCo₂O₄ (SHO); (e) NiCo₂O₄ (SBC). (f) Comparison of galvanostatic charge–discharge curves of the NiCo₂O₄ (SHO) and NiCo₂O₄ (SBC) electrodes at a current density of 5 A g⁻¹.

Table 2Comparison of the physicochemical property of NiCo₂O₄ prepared by various methods reported currently.

Samples	Synthetic methods	BET specific surface areas	Specific capacitance	Refs.
NiCo ₂ O ₄ aerogels	Sol–gel	122 m ² g ⁻¹	1400 F g ⁻¹ (25 mV s ⁻¹)	[4]
NiCo ₂ O ₄ nanoflakes	Chemical bath deposition	35 m ² g ⁻¹	330 F g ⁻¹ (1 A g ⁻¹)	[41]
NiCo ₂ O ₄ nanoplates	Hydrothermal	67.1 m ² g ⁻¹	294 F g ⁻¹ (1 A g ⁻¹)	[12]
NiCo ₂ O ₄ nanorods	Solid state reactions	71.7 m ² g ⁻¹	565 F g ⁻¹ (1 A g ⁻¹)	[42]
Network-like NiCo ₂ O ₄	Polymer-assisted chemical method	40 m ² g ⁻¹	587 F g ⁻¹ (2 A g ⁻¹)	[43]
NiCo ₂ O ₄ nanorods	Facial solution method	104.2 m ² g ⁻¹	1024 F g ⁻¹ (1 A g ⁻¹)	[5]
NiCo ₂ O ₄ nanoflakes	Co-precipitation	208 m ² g ⁻¹	1270 F g ⁻¹ (1 A g ⁻¹)	[44]
Mn substituted NiCo ₂ O ₄	Co-precipitation	/	110 F g ⁻¹ (1 A g ⁻¹)	[45]
Uniform porous NiCo ₂ O ₄	Co-precipitation	141.7 m ² g ⁻¹	726.8 F g ⁻¹ (1 A g ⁻¹)	This work

Fig. 6c shows the cyclic voltammograms of electrodes with different NiCo₂O₄ samples measured at a scan rate of 5 mV s⁻¹. It can be observed that the area of the NiCo₂O₄ (SBC) electrode under the CV curve is larger than the NiCo₂O₄ (SHO) electrode and the area of the Ni electrode could be almost negligible. As the specific capacitance is directly proportional to the area of the CV curve [39], the specific capacitance of NiCo₂O₄ (SBC) is higher than NiCo₂O₄ (SHO), which can be further confirmed by the following charge–discharge tests. The corresponding specific capacitance vs potential curves are provided in Fig. S2. In addition, the pair of redox peaks of the NiCo₂O₄ (SBC) electrode comes closer than the NiCo₂O₄ (SHO) electrode, demonstrating the better reversibility resulting from the NiCo₂O₄ (SBC) electrode.

Fig. 6f shows the galvanostatic charge–discharge curves of the NiCo₂O₄ (SHO) and NiCo₂O₄ (SBC) electrodes at the current density of 5 A g⁻¹ with a potential range from 0 to 0.5 V. Evidently, the NiCo₂O₄ (SBC) electrode exhibits a longer discharge time than the NiCo₂O₄ (SHO) electrode, which manifests the higher specific capacitance of the NiCo₂O₄ (SBC) electrode. Fig. 6d and e respectively display the galvanostatic charge–discharge curves of the NiCo₂O₄ electrodes prepared by NaOH and NaHCO₃ at various current densities. The nonlinear charge–discharge curves and the voltage plateaus could match well with the peaks observed from the CV curves, which further verifies the pseudocapacitive behavior of the NiCo₂O₄ electrodes. The specific capacitance of the NiCo₂O₄ electrodes can be calculated by using the following formula [40]:

$$C_m = (I \times \Delta t) / (m \times \Delta V) \quad (8)$$

where C_m (F g⁻¹) is the specific capacitance of a single electrode, I (A) is the discharging current, Δt (s) is the discharging time, ΔV (V) is the potential drop during discharge, and m (g) is the mass of active materials. Thus, the specific capacitance values of the NiCo₂O₄ electrodes prepared by different precipitants are calculated from the discharge curves. The NiCo₂O₄ (SBC) electrode exhibits the specific capacitances of 726.8, 726.4, 685, 622 and 500 F g⁻¹ at 1, 2, 5, 10 and 20 A g⁻¹, respectively, which are higher than those of the NiCo₂O₄ (SHO) electrode (667.6, 653.2, 564, 456 and 268 F g⁻¹ at 1, 2, 5, 10 and 20 A g⁻¹, respectively). And the physicochemical performance of NiCo₂O₄ (SBC) reported in this work is comparable with the other work reported recently [4,5,12,41–44,45] as shown in Table 2. Besides, the relationships between specific capacitance and current density are illustrated in Fig. 7a. It is worth noting that the NiCo₂O₄ (SBC) electrode also shows higher capacity retention rate (69%) than the NiCo₂O₄ (SHO) electrode (40%) when varying from 1 to 20 A g⁻¹, which indicates that the NiCo₂O₄ (SBC) electrode has better charge–discharge properties even at high current density. The high capacity retention rate of the NiCo₂O₄ (SBC) electrode could be ascribed to the larger pore volume and much narrower pore size distributions, of which facilitate to accommodate more electrolyte ions and provide faster ion and electron transportation channel [22].

The tests of long-term cycling stability of the NiCo₂O₄ (SHO) and NiCo₂O₄ (SBC) electrodes were conducted at a constant current

density of 5 A g⁻¹ in the potential range of 0–0.5 V in 2 M KOH solution for 2000 cycles. As shown in Fig. 7b, the specific capacitance of the two samples decreases rapidly in the first 500 cycles. Nevertheless, the NiCo₂O₄ (SBC) electrode stays almost unchanged in the following 1500 cycles while the NiCo₂O₄ (SHO) electrode decreases slowly and continuously. The specific capacitance of the NiCo₂O₄ (SBC) electrode is 704 F g⁻¹ in the first cycle and it decreases to 512 F g⁻¹ after 2000 times with a high retention of 72.7%, whereas the specific capacitance of the NiCo₂O₄ (SHO) electrode is 560 F g⁻¹ in the first cycle and it gradually decreases to 320 F g⁻¹ after 2000 times with a low retention of 57.1%. Therefore, we can estimate that the NiCo₂O₄ (SBC) electrode has better cycling stability in comparison with the NiCo₂O₄ (SHO) electrode. The better cycling stability may be ascribed to the differences in the pore structures as the uniform mesoporous structure with the larger pore volume facilitates to alleviate the volume changes during the fast charge–discharge process.

The EIS analysis can predict the behavior of electrochemical capacitor and determine the parameters affecting the performance of an electrode such as electrical conductivity, diffusion properties and charge-transfer properties [46]. The EIS tests were performed in 2 M KOH and the EIS data were analyzed by using Nyquist plots measured in the frequency range (100 kHz–0.1 Hz) as shown in Fig. 7c. In the high frequency area, the real axis intercept (Z') represents the internal resistance, including the contact resistance at the active material/current collector interface, the intrinsic resistance of the active material and the ionic resistance of the electrolyte, and the diameter of the semicircle corresponds to the charge transfer resistance [47]. In Nyquist plots, both of the NiCo₂O₄ electrodes demonstrate a small real axis intercept, indicating the low interfacial resistance between current collector and active material, electrolyte resistance and active material resistance. However, it is hard to judge those two inconspicuous semicircles of the two samples. Based on the similar EIS experiment conducted by Liu et al., it seems that the semicircles of NiCo₂O₄ (SBC) electrode could exhibit smaller diameter than that of the NiCo₂O₄ (SHO) electrode [48]. In the low frequency region, the linear part corresponds to the Warburg impedance (W) and it could be described as a diffusive impedance within the host material. The Nyquist plot is a vertical curve for an ideal capacitive material. The more vertical the curve is, the better the capacitive behavior is [49]. Compared with the NiCo₂O₄ (SHO) electrode, the NiCo₂O₄ (SBC) electrode shows more vertical curve leaning to imaginary axis more than 45° at a low frequency area, indicating the more facile electrolyte ions diffusion to the active material and more ideal capacitor behavior because of its unique loose mesoporous structure.

4. Conclusion

In summary, the uniform porous NiCo₂O₄ was fabricated by a co-precipitation method using NaHCO₃ as precipitant, which shows a great benefit over NiCo₂O₄ prepared by NaOH in electro-

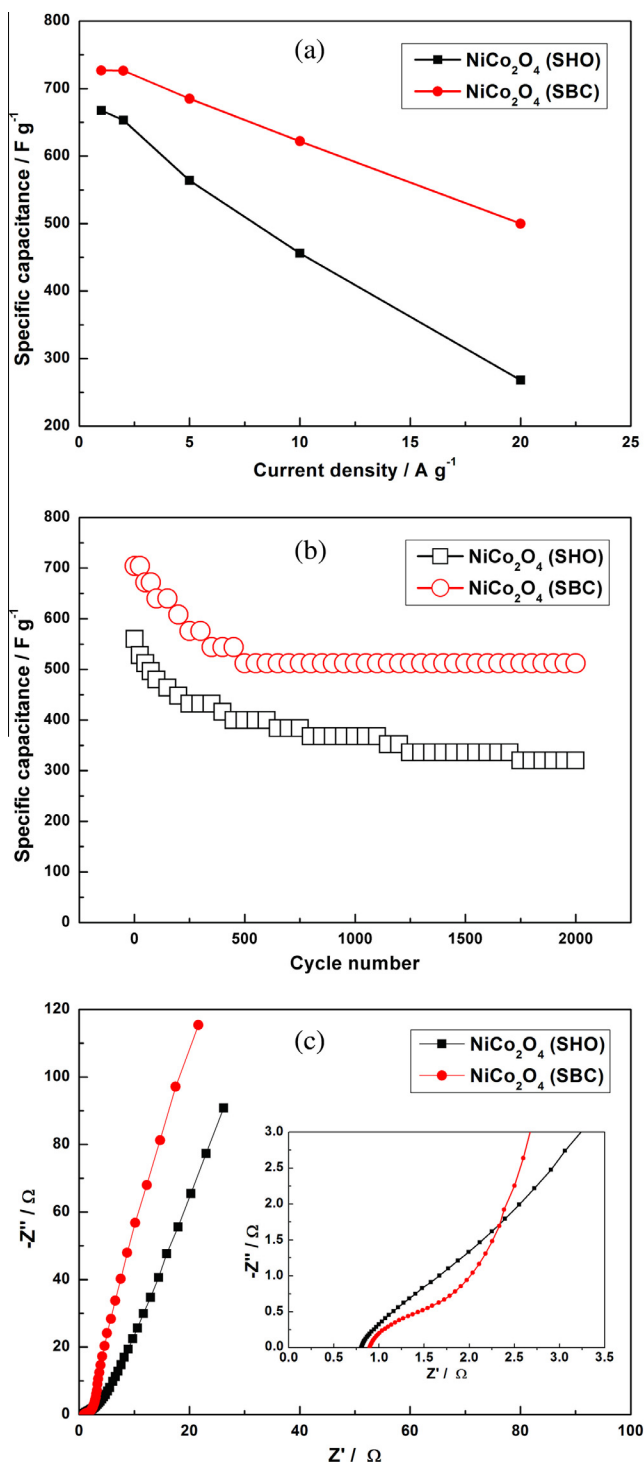


Fig. 7. (a) Comparison of the specific capacitance change of the NiCo₂O₄ (SHO) and NiCo₂O₄ (SBC) electrodes as a function of current density; (b) comparison of the cycling stability of the NiCo₂O₄ (SHO) and NiCo₂O₄ (SBC) electrodes at a current density of 5 A g⁻¹; (c) comparison of Nyquist impedance plots of the NiCo₂O₄ (SHO) and NiCo₂O₄ (SBC) electrodes, and the inset shows a magnification of the high-frequency region of the impedance spectra.

chemical performances, including specific capacity, rate retention and cycle stability. The loose mesoporous structure with higher surface area and larger pore volume facilitates to fast electrolyte ion diffusion and charge transfer, demonstrating improved specific capacitance of 726.8 F g⁻¹ at a current density of 1 A g⁻¹ and better cycle stability of 72.7% retention at a current density of 5 A g⁻¹

after 2000 cycles. The capacity retention rate of the NiCo₂O₄ (SBC) electrode is as high as 69% compared to the NiCo₂O₄ (SHO) electrode of 40% varying from 1 to 20 A g⁻¹. It is closely related to the addition of NaHCO₃ which contributes to prevent agglomeration of the nanoparticles, and thus forming well-distributed mesoporous NiCo₂O₄. These results indicate that utilizing NaHCO₃ as precipitant for synthesizing NiCo₂O₄ has a great advantage over NaOH, which is of great significance for further improvement of the electrochemical performance of NiCo₂O₄-based supercapacitors. In addition, using this kind of simple, facile method has great advantage in achieving large scale commercial application. We can also apply this method in preparing other metal oxides with great interest.

Acknowledgments

The work is financially supported by National Natural Science Foundation of China (21473258), National Basic Research Program of China (2014CB643401), Distinguished Young Scientists of Hunan Province (13JJ1004), Program for the New Century Excellent Talents in University (NCET-11-0513), and Hunan Provincial Innovation Foundation for Postgraduate (CX2013B048).

Appendix A. Supplementary material

Supplementary data associated with this article can be found, in the online version, at <http://dx.doi.org/10.1016/j.jallcom.2015.01.147>.

References

- [1] P. Simon, Y. Gogotsi, *Nat. Mater.* 7 (2008) 845–854.
- [2] C. Yuan, H.B. Wu, Y. Xie, X.W.D. Lou, *Angew. Chem. Int. Ed.* 53 (2014) 1488–1504.
- [3] Z. Wu, Y. Zhu, X. Ji, *J. Mater. Chem. A* 2 (2014) 14759–14772.
- [4] T.Y. Wei, C.H. Chen, H.C. Chien, S.Y. Lu, C.C. Hu, *Adv. Mater.* 22 (2010) 347–351.
- [5] G. Zhang, X.W.D. Lou, *Sci. Rep.* 3 (2013) 1–6.
- [6] C.-C. Hu, W.-C. Chen, *Electrochim. Acta* 49 (2004) 3469–3477.
- [7] C. Yuan, J. Li, L. Hou, J. Lin, G. Pang, L. Zhang, L. Lian, X. Zhang, *RSC Adv.* 3 (2013) 18573–18578.
- [8] X.-F. Lu, D.-J. Wu, R.-Z. Li, Q. Li, S.-H. Ye, Y.-X. Tong, G.-R. Li, *J. Mater. Chem. A* 2 (2014) 4706–4713.
- [9] Q. Zhang, Y. Deng, Z. Hu, Y. Liu, M. Yao, P. Liu, *Phys. Chem. Chem. Phys.* 16 (2014) 23451–23460.
- [10] N. Linares, A.M. Silvestre-Albero, E. Serrano, J. Silvestre-Albero, J. García-Martínez, *Chem. Soc. Rev.* 43 (2014) 7681–7717.
- [11] S. Kondrat, C. Perez, V. Presser, Y. Gogotsi, A. Kornyshev, *Energy Environ. Sci.* 5 (2012) 6474–6479.
- [12] J. Pu, J. Wang, X. Jin, F. Cui, E. Sheng, Z. Wang, *Electrochim. Acta* 106 (2013) 226–234.
- [13] C.-T. Hsu, C.-C. Hu, *J. Power Sources* 242 (2013) 662–671.
- [14] Q. Lu, Y. Chen, W. Li, J.G. Chen, J.Q. Xiao, F. Jiao, *J. Mater. Chem. A* 1 (2013) 2331–2336.
- [15] J. Li, S. Xiong, Y. Liu, Z. Ju, Y. Qian, *ACS Appl. Mater. Interfaces* 5 (2013) 981–988.
- [16] R. Ding, L. Qi, M. Jia, H. Wang, *Electrochim. Acta* 113 (2013) 290–301.
- [17] C. Wang, X. Zhang, D. Zhang, C. Yao, Y. Ma, *Electrochim. Acta* 63 (2012) 220–227.
- [18] R. Ding, L. Qi, H. Wang, *J. Solid State Electrochem.* 16 (2012) 3621–3633.
- [19] B. Chi, J. Li, Y. Han, Y. Chen, *Int. J. Hydrogen Energy* 29 (2004) 605–610.
- [20] S. Verma, H.M. Joshi, T. Jagadale, A. Chawla, R. Chandra, S. Ogale, *J. Phys. Chem. C* 112 (2008) 15106–15112.
- [21] S.-K. Chang, K.-T. Lee, Z. Zainal, K.-B. Tan, N.A. Yusof, W.M.D.W. Yusoff, J.-F. Lee, N.-L. Wu, *Electrochim. Acta* 67 (2012) 67–72.
- [22] H. Jiang, J. Ma, C. Li, *Chem. Commun.* 48 (2012) 4465–4467.
- [23] Z.-A. Hu, Y.-L. Xie, Y.-X. Wang, H.-Y. Wu, Y.-Y. Yang, Z.-Y. Zhang, *Electrochim. Acta* 54 (2009) 2737–2741.
- [24] Y. Zhu, X. Ji, Z. Wu, W. Song, H. Hou, Z. Wu, X. He, Q. Chen, C.E. Banks, *J. Power Sources* 267 (2014) 888–900.
- [25] R. Ding, L. Qi, M. Jia, H. Wang, *Nanoscale* 6 (2014) 1369–1376.
- [26] Z. Zhang, Y. Zheng, Y. Ni, Z. Liu, J. Chen, X. Liang, *J. Phys. Chem. B* 110 (2006) 12969–12973.
- [27] C.-C. Tseng, J.-L. Lee, Y.-M. Liu, M.-D. Ger, Y.-Y. Shu, *J. Taiwan Inst. Chem. Eng.* 44 (2013) 415–419.
- [28] Y. Wang, Y. Lei, J. Li, L. Gu, H. Yuan, D. Xiao, *ACS Appl. Mater. Interfaces* 6 (2014) 6739–6747.

- [29] B. Lefez, P. Nkeng, J. Lopitiaux, G. Poillerat, *Mater. Res. Bull.* 31 (1996) 1263–1267.
- [30] Y. Otsubo, K. Yamaguchi, *Chem. Soc. Jpn., Pure Chem. Sect.* 82 (1961) 557–560.
- [31] K. Kabiri, H. Omidian, S. Hashemi, M. Zohuriaan-Mehr, *Eur. Polymer J.* 39 (2003) 1341–1348.
- [32] K. Kabiri, H. Omidian, M. Zohuriaan-Mehr, *Polym. Int.* 52 (2003) 1158–1164.
- [33] X.-F. Wang, Z. You, D.-B. Ruan, *Chin. J. Chem. Phys.* 19 (2006) 341–346.
- [34] M.T. Li, Q.S. Fu, R.S. Yang, H. Wang, *Adv. Mater. Res.* 910 (2014) 7–10.
- [35] S. Xiong, J.S. Chen, X.W. Lou, H.C. Zeng, *Adv. Funct. Mater.* 22 (2012) 861–871.
- [36] J. Haenen, W. Visscher, E. Barendrecht, *J. Electroanal. Chem. Interfacial Electrochem.* 208 (1986) 273–296.
- [37] Y. Li, P. Hasin, Y. Wu, *Adv. Mater.* 22 (2010) 1926–1929.
- [38] Y. Chen, B. Qu, L. Hu, Z. Xu, Q. Li, T. Wang, *Nanoscale* 5 (2013) 9812–9820.
- [39] J.W. Lee, A.S. Hall, J.-D. Kim, T.E. Mallouk, *Chem. Mater.* 24 (2012) 1158–1164.
- [40] Y.Q. Wu, X.Y. Chen, P.T. Ji, Q.Q. Zhou, *Electrochim. Acta* 56 (2011) 7517–7522.
- [41] R.R. Salunkhe, K. Jang, H. Yu, S. Yu, T. Ganesh, S.-H. Han, H. Ahn, *J. Alloys Comp.* 509 (2011) 6677–6682.
- [42] Y. Zhu, X. Pu, W. Song, Z. Wu, Z. Zhou, X. He, F. Lu, M. Jing, B. Tang, X. Ji, *J. Alloys Comp.* 617 (2014) 988–993.
- [43] C. Yuan, J. Li, L. Hou, J. Lin, X. Zhang, S. Xiong, *J. Mater. Chem. A* 1 (2013) 11145–11151.
- [44] I. Shakir, M. Sarfraz, U.A. Rana, M. Nadeem, M.A. Al-Shaikh, *RSC Adv.* 3 (2013) 21386–21389.
- [45] S.K. Chang, K.T. Lee, Z. Zainal, K.B. Tan, N.A. Yusof, W.M.D.W. Yusoff, J.F. Lee, N.L. Wu, *Electrochim. Acta* 67 (2012) 67–72.
- [46] M.-S. Wu, M.-J. Wang, J.-J. Jow, *J. Power Sources* 195 (2010) 3950–3955.
- [47] Z. Fan, J. Yan, T. Wei, L. Zhi, G. Ning, T. Li, F. Wei, *Adv. Funct. Mater.* 21 (2011) 2366–2375.
- [48] X. Liu, S. Shi, Q. Xiong, L. Li, Y. Zhang, H. Tang, C. Gu, X. Wang, J. Tu, *ACS Appl. Mater. Interfaces* 5 (2013) 8790–8795.
- [49] M.D. Stoller, S. Park, Y. Zhu, J. An, R.S. Ruoff, *Nano Lett.* 8 (2008) 3498–3502.